Colloids and Surfaces A: Physicochemical and Engineering Aspects 718 (2025) 136864

Contents lists available at ScienceDirect

Colloids and Surfaces A: Physicochemical and Engineering Aspects

journal homepage: www.elsevier.com/locate/colsurfa

Tunable assembly of mixed PLGA-lipid nanoparticles via monoolein with improved reactive oxygen species cell protection

Cristina Minnelli [a], Francesco Spinozzi [a], Paolo Moretti [a], Giovanna Mobbili [a], Elena Romagnoli [a], Eleonora Pavoni [b], Elaheh Mohebbi [b], Brenda Romaldi [c], Tatiana Armeni [c], Pierluigi Stipa [b], Emiliano Laudadio [b,*]

[a] Department of Life and Environmental Sciences, Polytechnic University of Marche, Ancona, Italy
[b] Department of Science and Engineering of Matter, Environment and Urban Planning, Polytechnic University of Marche, Ancona, Italy
[c] Department of Specialized Clinical and Dental Sciences, Polytechnic University of Marche, Ancona, Italy

GRAPHICAL ABSTRACT

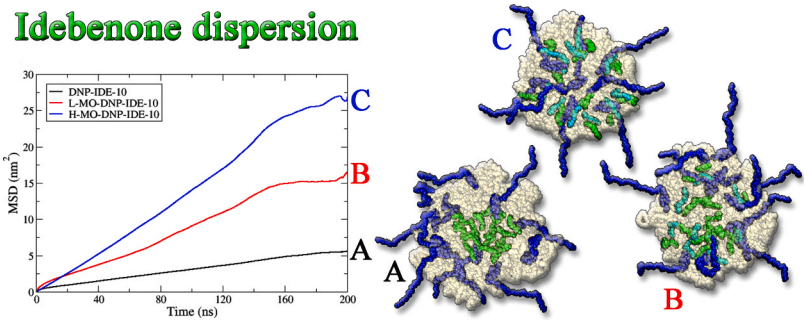

ARTICLE INFO

Keywords:
Lipid
PLGA
Antioxidants

ABSTRACT

Oxidative stress leads to pathologies such as photodamaged skin, psoriasis, and hyperpigmentation. Polymeric nanoparticles based on Poly-lactic-co-glicolic acid (PLGA) containing Idebenone improve its penetration into target skin cells reducing the level of free radicals. Despite these advantages, the lack of knowledge of endogenous barriers hinders the design of nanoparcticles. To address this problem, hybrid polymeric nanoparcticles with lipid components can improve stability and cellular internalization, increasing the antioxidant amount inside the cell. In this work, we designed and tested new mixed nanoformulations based on PLGA to deliver Idebenone using two lipid stabilizers as Monoolein (MO) and 2-distearoyl-sn-glycero-3-phosphoethanol-amine-polyethylene glycol-2000 (DSPE-PEG_{2000}). Atomic Force Microscopy and Dynamic Light Scattering noted the crucial role of the monoolein concentration in defining the size and the shape of the nanoparcticles. Small-angle X-ray Scattering and Molecular Dynamics simulations evidenced the interactions between monoolein and Idebenone to lead to a homogeneous arrangement at the nanoscale. The Electron Paramagnetic Resonance together with Density Functional Theory confirmed protection rate of nanoformulations against $OH^{\cdot}$ radicals. Cytotoxicity and flow cytometry confirmed that nanoparcticles with high and low monoolein concentrations scavenge

* Corresponding author.
E-mail address: e.laudadio@staff.univpm.it (E. Laudadio).

https://doi.org/10.1016/j.colsurfa.2025.136864
Received 29 December 2024; Received in revised form 2 April 2025; Accepted 6 April 2025
Available online 10 April 2025

reactive oxygen species (ROS) with greater efficacy than Idebenone alone. This scavenging ability indicates that the presence of nanoparcticles enhances the Idebenone's adsorption and cell protection from oxidative stress.

1. Introduction

In the last years, many different nanoparticles (NPs) have been developed to design efficient drug delivery systems. [1–6] These formulations consist of a vector and a series of stabilizing molecules, allowing to find the best conditions to protect small molecules from metabolic processes and then to deliver them to the target site. More recently, the use of polymers to design NPs opened to a wide range of possible applications. This is thanks to the enormous variety of chemical and biological functionalities that can be incorporated into polymeric NPs designs, controlling their size, shape, and surface charge [7]. NPs based on polyester cores already represent FDA-approved products [8, 9], and among them, the copolymer poly(lactic-co-glycolic acid) (PLGA) (Fig. 1**A**) is currently the most used one [1,3,10]. In fact, PLA is slightly more hydrophobic and resistant to hydrolytic degradation than PGA, and the hydrophobicity and degradation profile of the copolymer can be tuned by modulating the PLA:PGA ratio. This makes PLGA a highly customizable copolymer [11–13].

Idebenone (IDE) (Fig. 1**B**) is a synthetic analogue of ubiquinone (also known as Coenzyme Q10) which increases ATP production for the mitochondrial functions [14]. It can also reduce free radicals, inhibit lipid peroxidation, and then protect the lipid membrane and mitochondria from oxidative damage [15]. IDE contains a redox-active quinone moiety that can donate electrons to detoxify radicals [16]. This means that the intrinsic antioxidant function of IDE is dependent on two-electron reduction to Idebenol without the creation of unstable intermediates. On the other hand, instead of being a direct antioxidant, it's well known that IDE also increases the ability of cells to counteract oxidative stress by upregulating their physiological defense mechanisms, then decreasing again the production of oxidative radicals [17–19]. Given its potent antioxidant properties, IDE has attracted considerable interest in treating various oxidative stress-related disorders. However, its poor water solubility, stability, and bioavailability often hampered its clinical and therapeutic potential. Drug delivery technologies and formulation strategies appear to be crucial in overcoming these limitations, maximising the beneficial properties of IDE. In this context, topical skincare formulations containing IDE show promise for treating photodamaged skin [20], psoriasis, skin aging, and hyperpigmentation [21]. NPs improve IDE penetration into target skin cells compared to non-encapsulated forms and therefore the ability to reduce free radicals' levels which is critical in preventing cellular damage and aging.

The development of IDE formulations based on PLGA nanoparticles has never been investigated. However, it is important to consider the chemical properties of IDE (LogP 4.3, aqueous solubility 7.5 $\times 10^{-3}$ mg/mL) which could guide the choice of stabilizers used during the NPs fabrication.

Within this framework, we recently demonstrated that 2-distearoyl-sn-glycero-3-phosphoethanol-amine-poly(ethylene glycol (DSPE-PEG_{2000}) (Fig. 1**C**) as a stabilizer for PLGA NPs provides significant advantages over polyvinyl alcohol (PVA) in presence of lipophilic drug, particularly in terms of stability, and enhanced drug delivery capabilities [1]. Furthermore, it is well established that PEGylated lipids demonstrate lower immunogenicity than PVA-based NPs when administered intravenously [22]. This is because the PEG moiety creates a 'stealth' layer around the nanoparticles, effectively reducing their recognition by the immune system. In this perspective, the present work introduces the design and development of a novel PLGA-IDE NPs prepared using DSPE-PEG_{2000} as a stabilizer and employing monoolein (MO) in the self-assembly process. MO's unique structure, consisting of a lipid with a single unsaturated fatty acid chain attached to a glycerol backbone (Fig. 1**D**), led to the formation of colloidal stable and effective ROS-scavenging NPs. The influence of MO on the PLGA NP's properties has been therefore deeply investigated using a combined *in silico* and *in vitro* approach. Full-atom molecular dynamics (MD) simulations have been performed to remark on the different self-assembly processes of components and the interactions that guided the IDE insertion inside the PLGA matrix. Dynamic light scattering (DLS), AFM and SAXS have been used to deeply characterize the developed NPs. The encapsulation of IDE in the PLGA NPs has been evaluated both with and without MO by

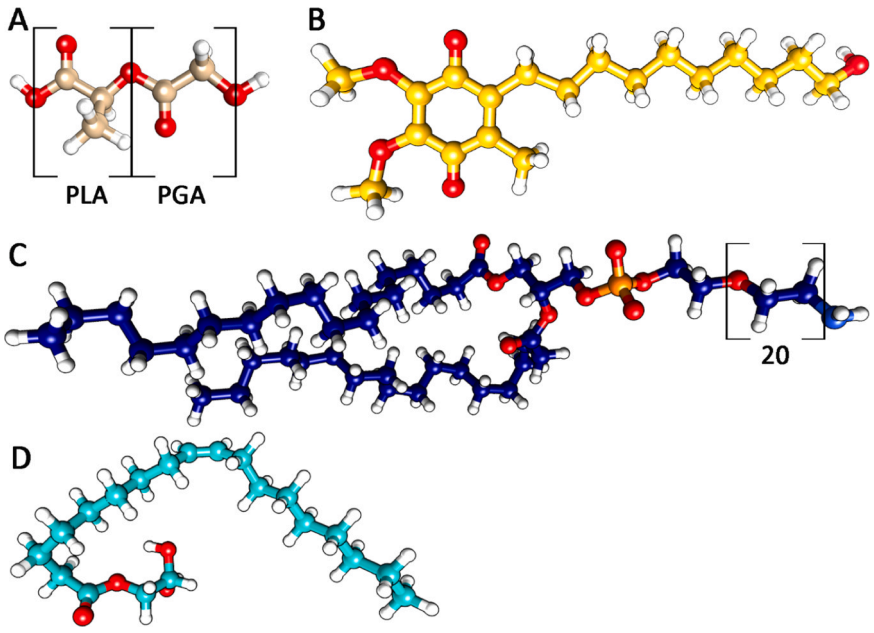

Fig. 1. 3D structures of PLGA (**A**), IDE (**B**), DSPE-PEG_{2000} (**C**), and MO (**D**). O, P, N, and H atoms are reported in red, orange, light blue, and white respectively. The C atoms color changes in relation to the chemical structure; brown (PLGA), goldenrod (IDE), cyan (MO), and dark blue (DSPE-PEG_{2000}).

experimental measurements and *in silico* calculation of the binding free energy. Finally, the ability of NPs to scavenge ROS has been demonstrated by electron paramagnetic resonance (EPR) spectroscopy experiments and *in vitro* studies with skin fibroblasts. The proposed combination between experimental and computational techniques provided important insights into the behavior of both PLGA NPs alone and with the IDE, yielding useful guidelines for the successful production of the systems to be used to treat pathologies associated with oxidative stress.

2. Materials and methods

2.1. Materials

Poly-lactic-co-glicolic acid (PLGA), 2-distearoyl-sn-glycero-3-phosphoethanol-amine-polyethylene glycol-2000 (DSPE-PEG_{2000}), Monoolein (MO, ≥99 %), Idebenone (IDE, ≥98 % HPLC), 5,5-Dimethyl-1-pyrroline N-oxide (DMPO, ≥98 % GC), ferrous sulfate ($FeSO_4$), sephadex G-50, 3-(4,5-dimethylthiazol-2-yl-2,5-diphenyl tetrazolium bromide (MTT), hydrogen peroxide and all solvents were obtained from Merck (Stenheim, Germany). All the solutions were prepared in ultrapure MilliQ water. Human Dermal Fibroblast (HDF) cells (CLS Cell Lines Service GmbH, No. 300606) were obtained from American Type Culture Collection (ATCC) Manassas, Virginia, USA. All cell culture reagents were purchased from Euroclone (Euroclone, Italy).

2.2. Preparation of PLGA-DSPE-PEG_{2000} and PLGA-MO-DSPE-PEG_{2000} NPs

PLGA-DSPE-PEG_{2000} NPs (DNP) were prepared following our previously reported procedure [1] with slight modifications. First, aqueous solution (water phase) containing 2 % DSPE-PEG_{2000} was prepared and warmed at 70°C for 30 minutes. For the preparation of DNPs containing IDE, an appropriate amount of IDE solution in ethanol was added to the pre-warmed DSPE-PEG_{2000} water phase and allowed to equilibrate for additional 30 min to obtain a final IDE concentration of 10 % and 15 % w/w of total NPs. 40 mg of PLGA was dissolved in 12 mL of acetone (organic phase), and then, it was added dropwise to 12 mL of water phase containing DSPE-PEG_{2000} in the presence or not of IDE obtaining DNP, DNP-IDE10 and DNP-IDE15, respectively. When the mixture of a volatile non-water miscible solvent and an aqueous solution was formed, it was emulsified by sonication using an ultrasonicator (Qsonica Q125) at 30 % amplitude for 30 s. The obtained oil-in-water emulsion was magnetically stirred for 6 h at 60 °C until the organic solvent completely evaporated.

For the preparation of PLGA-MO-DSPE-PEG_{2000}, two different MO concentrations were used: 2.2 % or 4.4 % w/w of MO designed as low (L-MO-DNP) and high (H-MO-DNP) MO concentration, respectively. An appropriate amount of MO in methanol was added to the water phase containing DSPE-PEG alone (L-MO-DNP and H-MO-DNP) or DSPE-PEG and IDE (L-MO-DNP-IDE10, H-MO-DNP-IDE10, L-MO-DNP-IDE15 and H-MO-DNP-IDE15) followed by the same protocol used for the preparation of DNPs.

The not encapsulated IDE was removed by gel exclusion chromatography following a well-established procedure for PLGA NPs [1,2]. The percentage of IDE loaded inside the NP (drug loading, %) and the encapsulation efficiency (EE, %) of all formulations were determined by the measurement of IDE concentration in purified and impurified nanoparticles after lysis with DMSO by spectrophotometric analyses at λ= 284 nm. All experiments were repeated at least three times, and measurements were carried out in triplicate.

The EE % and drug loading % were calculated using the following equations:

EE (%) = (amount of IDE inside NPs/initial amount of IDE added) x100

Drug loading (%) = amount of IDE inside NPs/total weight of NPs

2.3. Characterization

2.3.1. Dynamic light scattering

The intensity-based diameter (Z-average), the polydispersity index (PDI) and zeta potential of PLGA NPs were measured by dynamic light scattering (DLS) and electrophoretic light scattering using Malvern Zetasizer Nano ZS (Malvern Instruments GmbH, Marie-Curie-Straβe 4/1, 71,083 Herrenberg, Germany). Measurements were performed at 25°C with a fixed angle of 173° in PBS at pH 7.4. The reported data represents the average of at least three different autocorrelations that were carried out for each sample.

2.3.2. Small-angle X-ray scattering

The Small-angle X-ray scattering (SAXS) data were collected at the BioSAXS beamline BM29 of ESRF, The European Synchrotron (Grenoble, France), using an X-ray wavelength (λ) of 0.992 Å (photon energy 12.5 keV). The scattering vector modulus, $q = 4\pi \sin\theta/\lambda$ (where 2θ is the scattering angle), ranged from 0.006 to 0.50 $Å^{-1}$. Measurements were performed at 25°C with a 1 mm diameter quartz capillary, having a wall thickness of a few tens of microns, and controlled by a robotic apparatus. Each measurement was obtained by averaging 20 independent frames collected at different positions within the capillary. Buffer measurements were taken both before and after each sample to enable accurate background subtraction. Absolute scale SAXS curves, represented as radially averaged macroscopic differential scattering cross sections ($d\Sigma/d\Omega$) as a function of q, were calibrated in cm^{-1} unit using MilliQ water as reference standard.

The SAXS data analysis was performed using the GENFIT software [23]. The data was best interpreted using a model of large core-shell polydisperse spheres primarily made of hydrated PLGA-DSPE-PEG_{2000}, within which lipid structures formed by MO are present. These lipid structures are locally cylindrical and organized into a sponge phase (L_3) [24]. According to literature [25,26] the scattering arising from the interaction between the internal ordered structure and the rest of the sphere is negligible, allowing for a simplified model.

Specifically, the SAXS curves were fitted using the following equation

$$\frac{d\Sigma}{d\Omega}(q) = n_s P_s(q) + n_c P_c(q) S(q) + B \quad (1)$$

In this equation, $P_s(q)$ represents the form factor of a sphere with a core electron density ρ_{core} surrounded by a shell with electron density ρ_{shell}. The sphere has an outer radius (R) and a shell thickness (δ), both of which are polydisperse. The polydispersity of R and δ is described by two Schulz distribution functions, $p(R)$ and $p(\delta)$, respectively. These distributions are characterized by the mean radius, $< R >$, and its dispersion, defined as $\xi_R = \left[1 - < R^2 > / < R >^2\right]^{1/2}$, where $< R^j > = \int R^j p(R) dR$. Similarly, the mean shell thickness, $< \delta >$, is characterized along with its dispersion, defined as $\xi_\delta = [1 - < \delta^2 > / < \delta >^2]^{1/2}$.

The electron densities ρ_{core} and ρ_{shell} are calculated by assuming distinct water volume fractions ($\Phi_{w,k}$) within the core and shell domains. These are calculated as $\rho_k = \rho_{dry}(1 - \Phi_{w,k}) + \rho_w \Phi_{w,k}$, where k refers to either core or shell. Here ρ_{dry} is the electron density of the dry components forming the nanoparticles ($\rho_{dry} = [\sum_i c_i \nu_i \rho_i / W_i] / [\sum_i c_i \nu_i / W_i]$, with c_i, W_i, ν_i and ρ_i representing the w/v concentration (mg/mL), molecular weight (Da), molecular volume ($Å^3$), and electron density ($e/Å^3$) of the i-th molecular group, respectively. ρ_w is the electron density of water.

The second term of Eq. 1 contains the form factor of a randomly oriented homogeneous cylinder, $P_c(q)$, which represents the repeat unit of the sponge. This is multiplied by the structure factor of L_3 sponge phase, $S(q) = 1 + K_S / [\xi_p^{-2} + \left(q - q_p\right)^2]$, which accounts for the broad

correlation peak centered at q_p with correlation length ξ_p (cit). The cylinder's dimensions are defined by its radius R_c and height H_c, while the sponge cell dimension is $L = 2\pi/q_p$. The remaining parameters of Eq. 1 include the number densities of the spheres (n_s) and the cylinders (n_c), the structure factor constant (K_S), and the flat background (B), which accounts for potential imperfections in buffer subtraction. It is helpful to express the number density of the spheres as a function of the volume fraction η_{dry} of the scattering material, a parameter assumed to be known, along with the geometrical parameters of the sphere according to $n_s = \eta_{dry}/[V_{core}(1-\Phi_{w,core}) + V_{shell}(1-\Phi_{w,shell})]$, where $V_{shell} = 4\pi[<\delta^3>/3 + <\delta^2><R> + <\delta><R^2>]$ and $V_{core} = 4\pi <R^3>/3 - V_{shell}$. Here the averages $<R^j>$ and $<\delta^j>$ are analytically calculated using the Schulz distribution function. The relationship between n_s and η_{dry} is important because, with SAXS data measured on an absolute scale, it serves as an additional constraint for the fitting parameters.

2.3.3. Atomic force microscopy

The atomic force microscopy (AFM) characterization has been made using Solver Pro P-47 (NT-MDT) equipped with an NSG03/Au tip (TipsNano). The samples were deposited on a mica surface and let dry for a few hours. The scans were obtained by semi-contact mode, with a tip resonance at about 95 kHz and 25 °C room temperature. The images obtained by the AFM analyses represent an area of 3 μm x 3 μm in the x and y directions.

2.4. In silico methods

Three systems were modelled and stabilized with a *in silico* approach based on Molecular Dynamics (MD) simulations. The formulations were listed below: PLGA-DSPE-PEG_{2000}-IDE (DNP-IDE-10), PLGA-DSPE-PEG_{2000}-MO-IDE (L-MO-DNP-IDE-10), and PLGA-DSPE-PEG_{2000}-MO2-IDE (H-MO-DNP-IDE-10). We decided to model only these three systems despite the large number of different formulations because they are representative of the three different behaviors in the presence of the tested concentration of IDE. For a complete and accurate comparison, the PLGA-DSPE-PEG_{2000} (DNP) system was also considered, although its modeling and characterization has been covered in our previous publication [1]. Each single component was optimized independently, and the needed amount of each compound was evaluated to be as close as possible to the experimental conditions. In this concern, a PLGA system composed by 7500 lactic units (LA) together with 2500 glycolic units (GA) was generated. To have the amorphous NPs, the LA components were considered in atactic way, and the GA units were randomly displaced along the copolymer chain. The three-dimensional structures of DSPE-PEG_{2000}, MO, and IDE molecules were generated and minimized using the semi-empirical AM1-BCC method [27]. Since the experimental concentrations are expressed in mg/mL, a simulation box was created around the PLGA dispersed system to include 942,564 TIP3P water molecules [28]. Then, 8 DSPE-PEG_{2000} molecules together with 12 IDE compounds were added in each formulation. Regarding the MO, no molecules were included in the DNP-IDE-10 formulation, while 6 and 12 monoolein compounds were present in the L-MO-DNP-IDE-10 and H-MO-DNP-IDE-10 systems respectively.

GROMACS 2023.3 software [29] together with CHARMM36 force field [30] were chosen for MD simulations. The three systems were first minimized by applying periodic box conditions (PBCs) in all directions. Each system was subjected to the steepest descent algorithm, and then, the final frame of minimization has been used as the input structure for further minimization runs based on the conjugate gradient algorithm [31]. The Verlet cutoff scheme was used together with the LINCS algorithm for the constraints [32]. All the systems underwent an equilibration step based on 5 ns of annealing. The Verlet cutoff scheme and the LINCS algorithm were used again together with the particle mesh Ewald (PME) method to treat the long-range interactions. A weak temperature coupling (Berendsen thermostat) with a time constant of 1 ps was applied to maintain the reference temperature (310 K) throughout the whole run. After the equilibration, a production step of 200 ns of MD simulation was performed for each system in an isothermal−isobaric (NPT) ensemble at 1 atm and 310 K. The analysis of the MD trajectories have been performed using VMD [33] and Chimera software [34], together with the tools included in the GROMACS package. The same approach using the same tools was used to model and characterize the DNP system in our previous work.

Finally, the antioxidant activity of IDE was investigated using density functional theory (DFT) approach. In detail, the frontier molecular orbitals were determined, then, the quinone (oxidized), hydroquinone (reduced), and semiquinone forms were exhaustively investigated. The capability to operate hydrogen atom transfer (HAT) was calculated using the B3LYP hybrid functional [35] in combination with 6–311 + +G (d,p) basis set.

2.5. Cellular cytotoxicity and quantification of intracellular ROS by dichlorodihydrofluorescein diacetate

For the cytotoxicity studies, human dermal fibroblasts (HDFs) were seeded in 96-well plates at 2.5×10^4/well to reach 80 % confluence after 24 h. Then, the medium from each well was replaced with fresh medium containing increasing concentrations of H-MO-DNP and L-MO-DNP series loaded or not loaded with IDE (H-MO-DNP, H-MO-DNP-IDE10, L-MO-DNP, L-MO-DNP-IDE10). The free IDE was added at concentrations equal to the IDE content in the NPs (IDE, 0.5–16 μM). After incubation for 24 h, XTT assay was used to assess the cell cytotoxicity.

To detect reactive oxygen species (ROS) in cells, the cell-permeant fluorogenic probe 2',7'-dichlorodihydrofluorescein diacetate (DCFDA) (Merck, cod. 287810) was used. Cells were seeded in 24-well plates at 1×10^4 to reach 80 % of confluence after 24 h. At this time, cells were treated in complete DMEM containing free IDE, H-MO-DNP-IDE10 and L-MO-DNP-IDE10 with a final IDE and nanoparticles concentration of 4 μM and 9 μg/mL, respectively for 3 h prior to treatment with 1 mM hydrogen peroxide (H_2O_2) for 1 h. Then, cells were detached by trypsinization and washed with PBS (pH 7.4) following by incubation with 10 μM dye solution in pre-warmed PBS for 40 min at 37°C protected from light. After centrifugation, the dye buffer was removed, and cells were washed again with PBS and analyzed by flow cytometry (FITC-channel, Ex: 488 nm/Em: 519 nm) in which at least 2500 cells for each sample were measured using the same settings. Results are elaborated with FCS 7 express and reported by using histogram subtraction statistics tool by using as control untreated cells (% Positive cells with respect to control).

2.6. Electron paramagnetic resonance

Hydroxyl radicals (HO•) were produced using the Fenton reaction with ferrous sulfate ($FeSO_4$) and hydrogen peroxide (H_2O_2) as previously described [1] following the reported equation [36]:

$$Fe^{2+} + H_2O_2 \rightarrow Fe^{3+} + OH^- + OH^{\bullet} \quad (1)$$

The 5,5-dimethyl-1-pyrroline N-oxide (DMPO) was used as a spin trap; then, the generated $HO^{\bullet}$ radicals were rapidly trapped to produce the $[DMPO\text{-}HO]^{\bullet}$ adduct, which is characterized by specific four-lines EPR signal. The adduct content was determined for the following solutions: control solution (including only DMPO), a solution with only IDE, a solution without IDE (H-MO-DNP) and the two systems H-MO-DNP-IDE and L-MO-DNP-IDE. Nanoparticles, stored at room temperature and protected from light, are utilized one week after their preparation. The EPR spectra were transformed by double integration to evaluate the total amount of radicals released after 5 min of incubation in each system. X-band EPR measurements were performed using a Bruker EMX/Xenon spectrometer system equipped with a microwave frequency

counter and an NMR Gaussmeter for field calibration. Quantitative estimations were done using the native (Xenon) spectrometer software. Experiments were performed in triplicates for three times and reported as the mean of [DMPO-HO]• adduct concentration ± standard deviation.

3. Results and discussions

3.1. Monoolein tunes colloidal stability and particle size of PLGA NPs

Encapsulating IDE in PLGA NPs offers several potential benefits, but there are also challenges and limitations associated with this process. In this context, fine-tuning the formulation parameters, such as composition, and stabilizers used in relation to the characteristic of the delivered drug can improve encapsulation efficiency and drug loading. To our knowledge, only two existing PLGA-IDE formulations have been reported in literature. The first one comes from the meticulous work of R. Varela-Fernandez and colleagues, which reported the synthesis of IDE-loaded PLGA-PVA microspheres for the treatment of Leber Hereditary Optic Neuropathy (LHON), with a particle size of approximately 50 μm [37]. The second work related to Ide-PLGA systems comes from Morilla-Lomena and her groups, which developed PLGA/vitamin E microspheres loaded with IDE and active proteins to increase the neuroprotective activity, with a particle size of approximately 30 μm [38]. In contrast, our design and development approach focused on creating smaller PLGA particles with high drug loading and colloidal stability. This approach has the purpose of increasing particles retention and, therefore, bioavailability, that is compromised by using microparticles. The hydrophobic nature of IDE enables it to readily interact with the hydrophobic core of PLGA NP as well as with the alkyl chain of lipids. Starting from our previous work, we first synthetized PLGA NPs by using DSPE-PEG_{2000} lipid as stabilizer (DNP). IDE was added at a concentration equivalent to 10 % w/w of NPs designed as DNP-IDE-10 (Table 1). As already reported [1] the empty system has a very low polydispersity index (PDI<0.1) and a particle size is about 110 nm, confirming the reproducibility of the preparation method. However, the inclusion of IDE resulted in the formation of larger particles, ranging from 800 to 1500 nm, which exhibited high instability. This was evident from the appearance of yellow precipitates within 24 hours of preparation (data not shown). Based on our findings, we theorized that DSPE-PEG_{2000} alone did not sufficiently stabilize IDE within NPs, unlike what was observed in our previous study encapsulating another lipophilic antioxidant. [1] This underline how the chemical-physical properties of drugs are important in the selection of NPs composition. Therefore, we explored the incorporation of an additional amphiphilic component to further enhance NPs colloidal stability. In this context, monoolein (MO) was chosen, which is a monoester of glycerol featuring a hydrophobic tail derived from oleic acid. This structural characteristic, with a small polar head and a hydrophobic tail, bears resemblance to the structure of IDE. This similarity could be beneficial as it might be an enhancer of the IDE interaction with the lipid shell of PLGA-based NPs. MO was used at 2.3 % or 4.6 % w/w of NPs leading to the production of IDE-loaded-NPs series containing low (L-MO-DNP) or high MO concentration (H-MO-DNP) (Table 1). The addition of MO induced a dose-dependent increase in particle size of DNP NPs of about 30 nm and 110 nm, respectively at low MO (L-MO-DNP) and high (H-MO-DNP) concentrations. For L-MO-DNP, the presence of 10 % w/w IDE (L-DNP-IDE-10) led to a further increase in mean diameter and NPs exhibited an average diameter of 240 nm with a low polydispersity index (PDI) reaching however 320 nm in particle size after storage for 1 month with the presence of a few aggregates (Table 1). Optimal results were achieved by increasing the concentration of MO (H-MO-DNP-IDE-10) which promoted the formation of smaller NPs with a particle size of about 160 nm and ensured colloidal stability also after 1 month of preparation.

NPs prepared by using IDE 15 % w/w of NPs mainly culminated in the formation of colloidal unstable NPs or flocculation in the absence of MO or in the presence of low MO concentration (DNP-IDE-15 and L-MO-DNP-IDE-15). Also in this case, smaller and more stable NPs were obtained by using high MO concentration (H-MO-DNP-IDE-15) (Table S1) highlighting the important role of MO lipid in tuning the self-assembly process of mixed PLGA-based NPs. However, after 1 month of preparation, the formation of a few precipitates was observed.

The encapsulation efficiency (EE %) in all two types of MO-containing DNP decreased from the lower to the higher IDE concentration (Table 1 **and** Table S1), while a progressive increase in the loading capacity (DL%) was observed. The decrease in EE % is related to the different starting concentrations of IDE, while DL% directly reflects the amount of total entrapped antioxidants with respect to the total NP's weight. Overall, the H-MO-DNP-IDE-15 showed a higher ability to load IDE and the EE % was about 40 % higher with respect to L-MO-DNP-IDE-15. Therefore, DL% resulted in being much higher when a higher MO concentration was used. However, considering the colloidal stability after storage and the particle size of the produced NPs, we selected formulations containing 10 % IDE, and then, the following studies are focused on these systems.

From a structural point of view, the Atomic Force Microscopy (AFM) characterization confirmed the trend observed by DLS measurements. The AFM results showed that the DNP system comprises small spherical-shaped nanoparticles (Fig. 2). The increase of the NPs size is evident in both the system containing the MO (L-MO-DNP) and even more in the respective structure containing IDE (L-MO-DNP-IDE-10). As attested by DLS, the addition of MO produced an expansion in terms of particle size that depends on the added amount of MO; in fact, in high (H-MO-DNP) concentration, particles are bigger than the respective L-MO-DNP. On the opposite side, adding IDE to the system H-MO-DNP stimulated the formation of small spherical-shaped systems (H-MO-DNP-IDE-10).

Table 1
Composition and DLS of formulations.

Nanoparticles (NPs)	IDE (w/w of NPs)	GMO (w/w of NPs)	Hydrodynamic Diameter (DH) (nm)		PDI (T = 0)	EE %	DL %
			T = 0	T = 1 month			
DNP	-	-	119 ± 5	107 ± 8	0.06 ± 0.02	-	-
DNP-IDE−10	10	-	820 ± 300	-	0.5 ± 0.02	-	-
L-MO-DNP	-	2.3	154 ± 35	162 ± 41	0.08 ± 0.06	-	-
L-MO-DNP-IDE−10	10	2.3	216 ± 27	320 ± 25[a]	0.12 ± 0.03	100	9.5
H-MO-DNP	-	4.6	226 ± 4	220 ± 3	0.08 ± 0.01	-	-
H-MO-DNP-IDE−10	10	4.6	157 ± 3	163 ± 2	0.012 ± 0.005	100	9.3

[a] Presence of some flocculates and aggregates over time

3.2. Self-assembly studies of PLGA mixed NPs

Focusing on the previously described variations, it seems that the type and amount of each component allow to modulate the particle size of the systems. To gain deeper insight into the interactions between the biological components, we focused on understanding the formation dynamics of this novel formulation and the effect of varying MO concentrations on the IDE-loaded NPs structure at atomistic and molecular levels by using SAXS technique and MD simulations.

The self-assembly studies were carried out highlighting how the systems prepared *in silico* exhibit very different characteristics, also remarking the key role of MO in determining the dimensions of the systems. As previously indicated, the DNP system, already extensively analyzed in our previous study [1] was included in the comparison. The DNP shows the shortest spherical radius and most compactness of the

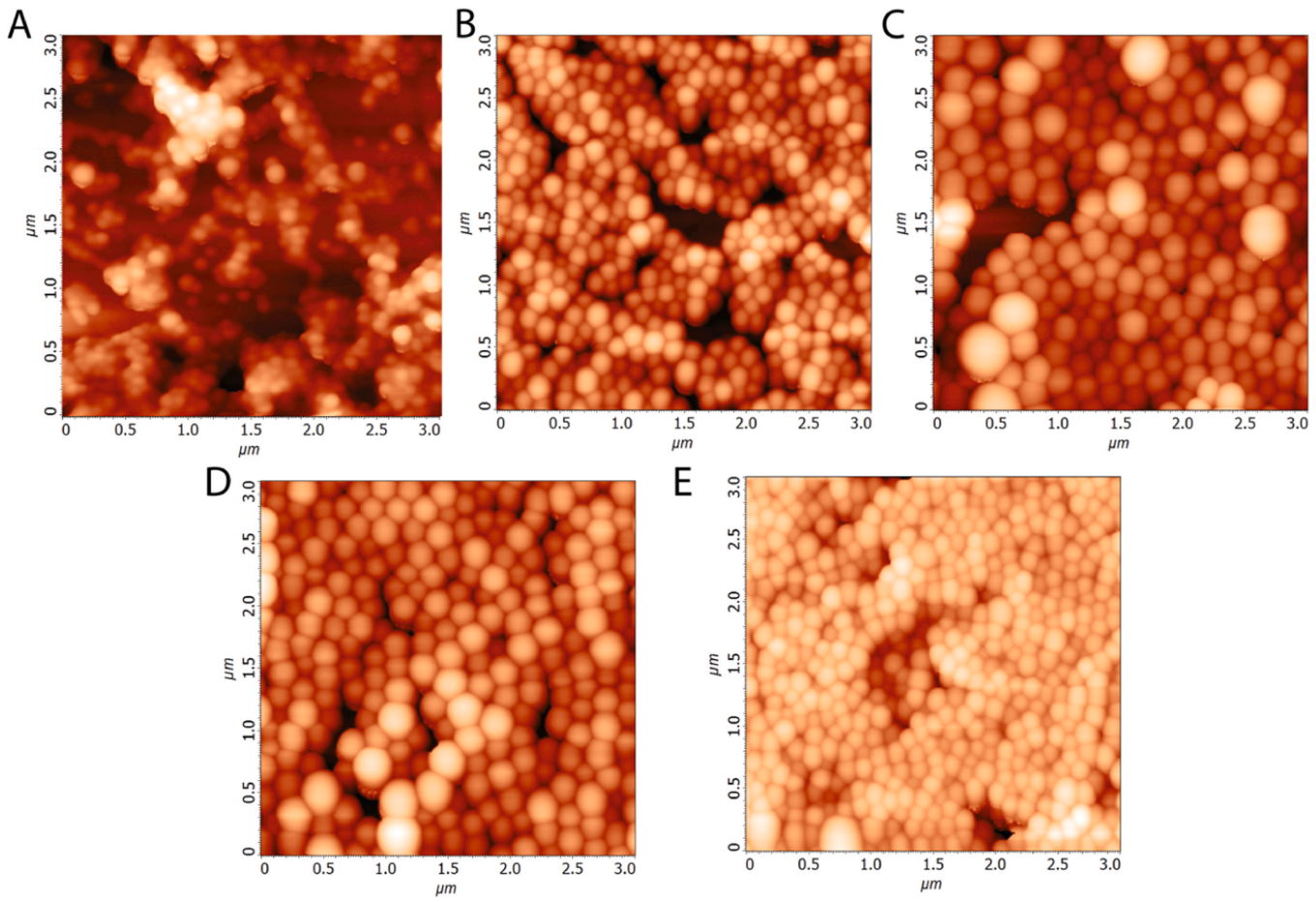

Fig. 2. AFM images of the systems: DNP (**A**), L-MO-DNP (**B**), L-MO-DNP-IDE-10 (**C**), H-MO-DNP (**D**) and H-MO-DNP-IDE-10 (**E**).

three modeled systems (Fig. 3**A**). The DNP-IDE-10 lacking MO, evolved into a disordered system with poorly defined shapes. Each IDE molecule generated a sort of dimers with itself in which the aliphatic chains always interacted, and some Hbonds were observed between the polar OH groups. These interactions stabilized the IDE in an aggregate which is located in the core of PLGA NP. This results in a system of particularly large dimensions, with a large surface area accessible to the solvent (Fig. 3**B**). With the addition of MO (L-MO-DNP-IDE-10), an evolution to a disordered binary-vesicle system was observed, where the MO diffused homogenously in the polymeric medium interacting with the aliphatic chain of the IDE molecules. The MO-IDE interactions seemed to be stronger than those observed in IDE-IDE and MO-MO, resulting in a more dispersed system in the PLGA medium, which also stabilized the entire NP leading to an ever-decreasing size (Fig. 3**C**). Finally, by further increasing the amount of monoolein (H-MO-DNP-IDE-10), the stabilizing role of MO molecules became even more evident. In fact, an ordered system was detected, and the IDE and MO molecules were dispersed equally in the polymeric medium without any aggregates (Fig. 3**D**). This led to a further decrease in the NP observed along the 200 ns of MD time, anyway, the direct comparison with the DNP clearly shows that the tendency of IDE molecules to interact with MO induces an increase in size of the NP, and MO seems to tune the NP size modulating and optimizing the dispersion of the IDE inside PLGA NP with a marked localization on the NP shell, escaping from the NP core.

The mean square displacement (MSD) of IDE in the PLGA matrix in function of the MD simulation time confirms the previous observations. This analysis is commonly used to identify the mode of displacement of particles over time. More in detail, MSD determines whether the particle is freely diffusing, transported, or bound and limited in its movement, providing a measure of its displacements in a medium. The results show a clear increase in the spread of IDEs from the core to the PLGA shell as the amount of MO increases (Fig. 4**A**).

Since both polar and apolar interactions were observed between the different components, Molecular Mechanics-Poisson Boltzmann surface area (MM-PBSA) was calculated to identify the driving force to lead to the NP in relation to the interactions along MD time (Fig. 4**B**). The results show that the apolar interaction is the most important feature to have a dispersed system, and this is also due to the hydrophilic character of the PLGA medium together with the presence of DSPE-PEG_{2000} molecules.

3.3. Small-angle X-ray scattering

The SAXS curves recorded at the BM29 beamline for the five samples of DNP, L-MO-DNP, H-MO-DNP, L-MO-DNP-IDE-10, H-MO-DNP-IDE-10 as log-log plots (Fig. 5). Notably, the curves for samples containing MO exhibit a subtle bump around 0.1 $Å^{-1}$, which was interpreted as a marker of the correlation length associated with the partially ordered structures typically formed by MO. The absence of additional well-defined correlation peaks at the expected positions for hexagonal or cubic phases suggests that this feature corresponds to the more disordered sponge phase. Additionally, at low q, the curves do not exhibit a slope close to zero, indicating the presence of dimensions approaching the detection limit of the q range used in these experiments ($2\pi/q_{min} \approx 1000$ Å). These observations informed the development of the SAXS model described in Section 2.2.2.

Using the composition of each sample, along with the estimated molecular volumes and electron densities of the molecular groups involved (Table 2), the volume fraction and average electron densities of the dry scattering material forming the NPs were calculated and used as

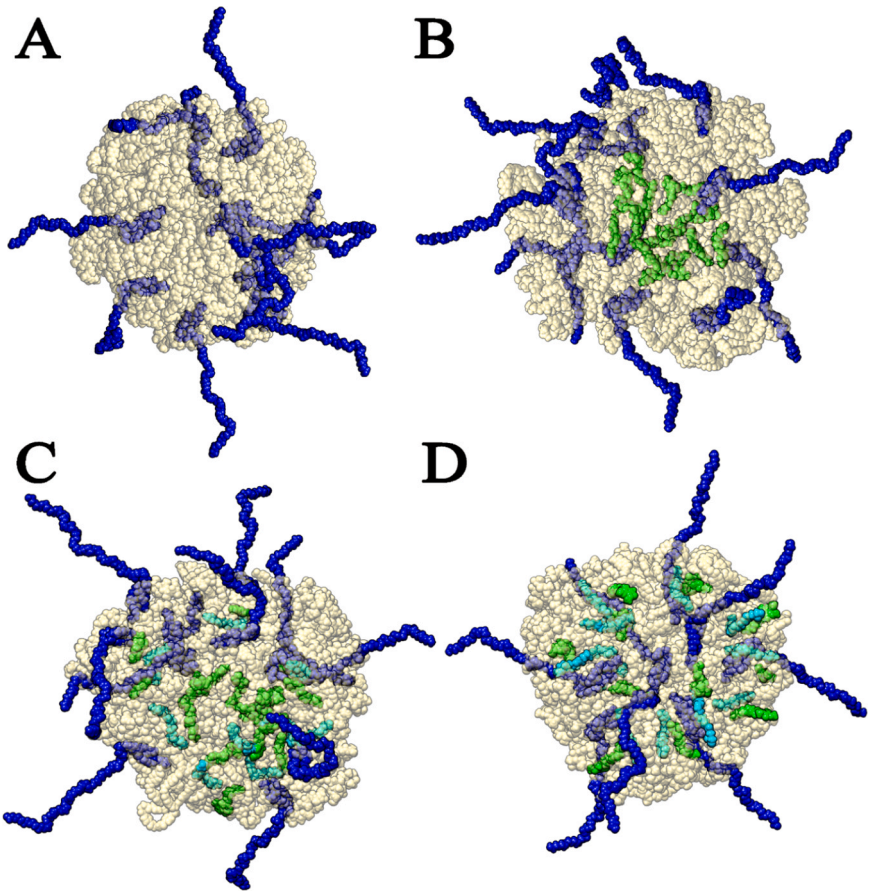

Fig. 3. Representative structures of the DNP (**A**), DNP-IDE-10 (**B**), L-MO-DNP-IDE-10 (**C**), and H-MO-DNP-IDE-10 (**D**) systems at the end of 200 ns of MD simulations. PLGA, DSPE-PEG$_{2000}$, MO, and IDE molecules are reported in yellow, blue, cyan, and green respectively.

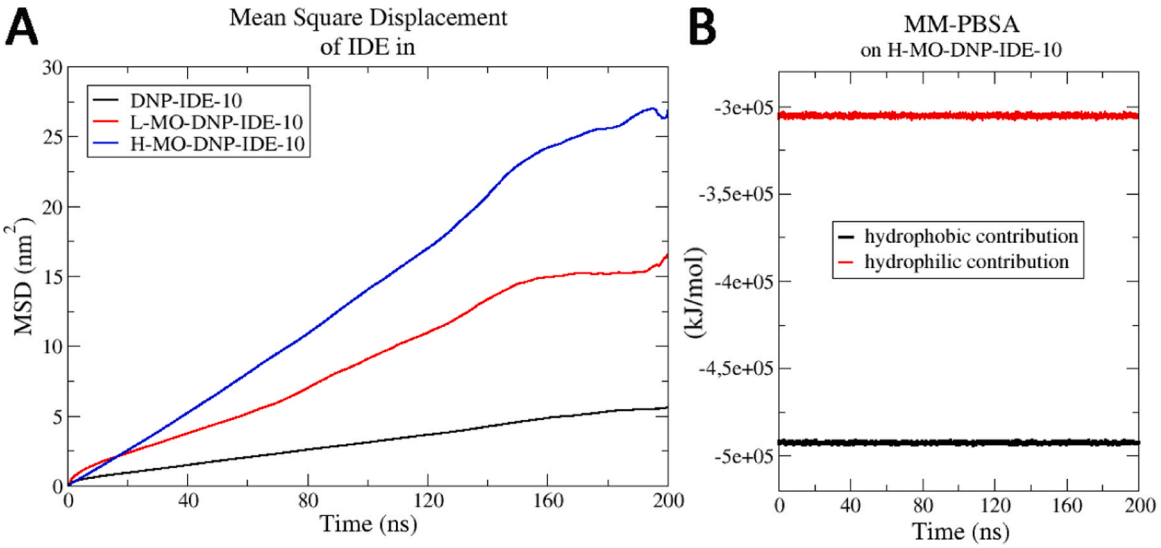

Fig. 4. Mean square displacement (MSD) of IDE molecules (**A**) and the Molecular Mechanics-Poisson Boltzmann surface area (MM-PBSA) of H-MO-DNP-IDE-10 (**B**).

fixed parameters in the data analysis procedure (Table 3).

The quality of the fit is not significantly affected by the radius (R_c) and height (H_c) of the cylinders representing the MO unit in the sponge phase. Therefore, these parameters were fixed at 15 Å.

Based on this assumption, we fitted each curve with the model presented in Sec. 2.2.2. The best fits are reported in Fig. 5 as solid red curves. In all cases, the quality of the fit is evident. Specifically, the fitted curves successfully capture the small negative curvature at low q, and, for Fig. 5**A-D**, they also reproduce the small oscillation occurring at $q \approx 0.02$ Å^{-1}

GENFIT optimizes all model parameters, including the flat background B, by employing a combination of methods such as Simulated Annealing and quasi-Newton algorithms. A robust estimation of parameter uncertainties is achieved by iteratively shifting all points of

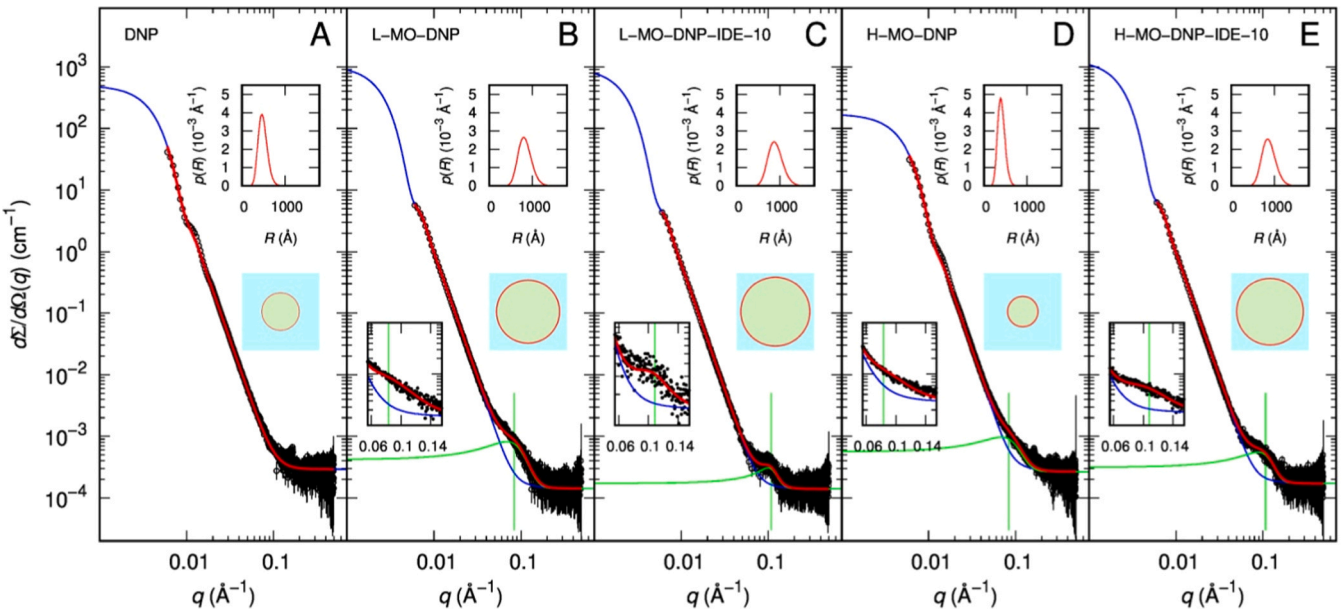

Fig. 5. SAXS data (black points with error bars) and corresponding best fit (solid red curves) for the samples DNP (**A**), L-MO-DNP (**B**), L-MO-DNP-IDE-10 (**C**), H-MO-DNP (**D**), and H-MO-DNP-IDE-10 (**E**). Solid blue and green curves represent the two contributions of Eq. 1: $n_s P_s(q)$ (polydisperse core-shell spheres) and $n_c P_c(q) S(q)$ (sponge phase), extended to a wider q range than that achieved in the experiments. The vertical green line marks the peak position q_p. The bottom insert in each panel shows a zoomed view of the q range from 0.06 to 0.14 Å^{-1}. The top insert presents the radial distribution functions $p(R)$ obtained from the best fits, while the central insert represents, in a box with side 2000 Å, the nanoparticle with radius $< R >$ and shell thickness $< \delta >$.

Table 2
Molecular volumes and electron densities of the chemical groups.

i-th group	ν_i (Å^3)	ρ_i (e/Å^3)
DSPE head[(a)]	323.3	0.433
DSPE tails[(a)]	957.8	0.286
MO head[(a)]	129.0	0.488
MO tail[(a)]	466.9	0.289
IDE head[(b)]	338.2	0.293
IDE tail[(b)]	318.5	0.279
PEG[(c)]	2939.1	0.371
PGA[(c)]	22681.5	0.417
PLA[(c)]	84490.2	0.426

(a) data calculated according to [39]; (b) data calculated according to [40]; (c) data calculated according to [41] considering the content of PGA and PLA in the PLGA copolymer

Table 3
Composition of the samples investigated with SAXS.

	MO	DSPE-PEG	PLGA	IDE	η_{dry}	ρ_{dry}
Sample	mg/mL				(‰)	(e/Å^3)
DNP	0.000	0.083	3.330	0.000	2.49	0.423
L-MO-DNP	0.075	0.083	3.330	0.000	2.56	0.420
L-MO-DNP-IDE−10	0.075	0.083	3.330	0.330	2.76	0.403
H-MO-DNP	0.150	0.083	3.330	0.000	2.64	0.418
H-MO-DNP-IDE−10	0.150	0.083	3.330	0.330	2.83	0.402

the SAXS curves within their standard deviations, repeating the minimization, and computing the mean value and standard deviation of each fitting parameter over 50 iterations. The most relevant parameters obtained from the analysis of SAXS data are reported in Fig. 6 as histograms with error bar. Regarding the mean radius of the sphere ($< R >$, Fig. 6**A**), the results show a progressive increase, nearly doubling from DNP (≈500 Å) to L-MO-DNP and L-MO-DNP-IDE-10. While the radius of the H-MO-DNP sample does not significantly differ from that of the DNP sample, the radius of the H-MO-DNP-IDE-10 sample reaches a value like that of the L-MO-DNP sample thereby confirming the results obtained by DLS and MD simulations (Table 1, Fig. 2). The effect of MO or IDE on the mean thickness of the spherical shell ($< \delta >$, Fig. 6**B**) is quite relevant: for the DNP sample it is slightly less than 20 Å, whereas for all the other cases it reaches similar values, around 30 Å. This increase is surely attributable to the MO and its ability to localize in proximity of the shell NPs. The dispersions of the sphere radius and the shell thickness are similar and around 0.2 (ξ_R and ξ_δ, Fig. 6**C-D**). The obtained Schulz distribution functions for the sphere radius are reported in the top-right insets in Fig. 5. The presence of water is insensitive on MO or IDE ($\Phi_{w,\text{core}}$ and $\Phi_{w,\text{shell}}$, Fig. 6**E-F**). For the core domain it is almost constant at 0.05, whereas for the shell it increases to 0.2. Regarding the structure of the sponge phase, the results indicate a more pronounced correlation in the sample L-MO-DNP, which exhibits the highest values of M_p, the peak height-to-background ratio (Fig. 6**G**). This suggests that IDE partially disrupts this ordered structure. Indeed, the correlation length (L, Fig. 6**H**) for both the L-MO-DNP and the H-MO-DNP sample is approximately 75 Å, whereas for the samples with IDE (L-MO-DNP-10 and H-MO-DNP-IDE-10) it decreases to about 60 Å. Finally, the peak correlation length (ξ_p, Fig. 6**I**) remains comprised between 20 and 30 Å, shorter than the repeating unit size (L). This suggests that the structural order breaks down over distances smaller than the characteristic cell dimension.

3.4. Protection toward HO• radical

Till now, the topological and structural aspects were discussed to determine differences in size, shape, and quantity of the antioxidant included in the NP. Since the aim of the work is to develop nanoformulations for the treatment of pathologies associated with oxidative stress, it is necessary to consider that different biological components can affect the effective reactivity of the system towards free radicals. For this purpose, the capability of each NP type to counteract the diffusion of HO• radical was quantified using EPR. The concentration of the [DMPO-HO]• adduct was determined for each system (Fig. 7**A-B**). In a control solution, any sample was included, and a 2.22×10^{-6} M of [DMPO-HO]• adduct was found (Table S2).

Focusing on the system containing H-MO-DNP, as expected, it did

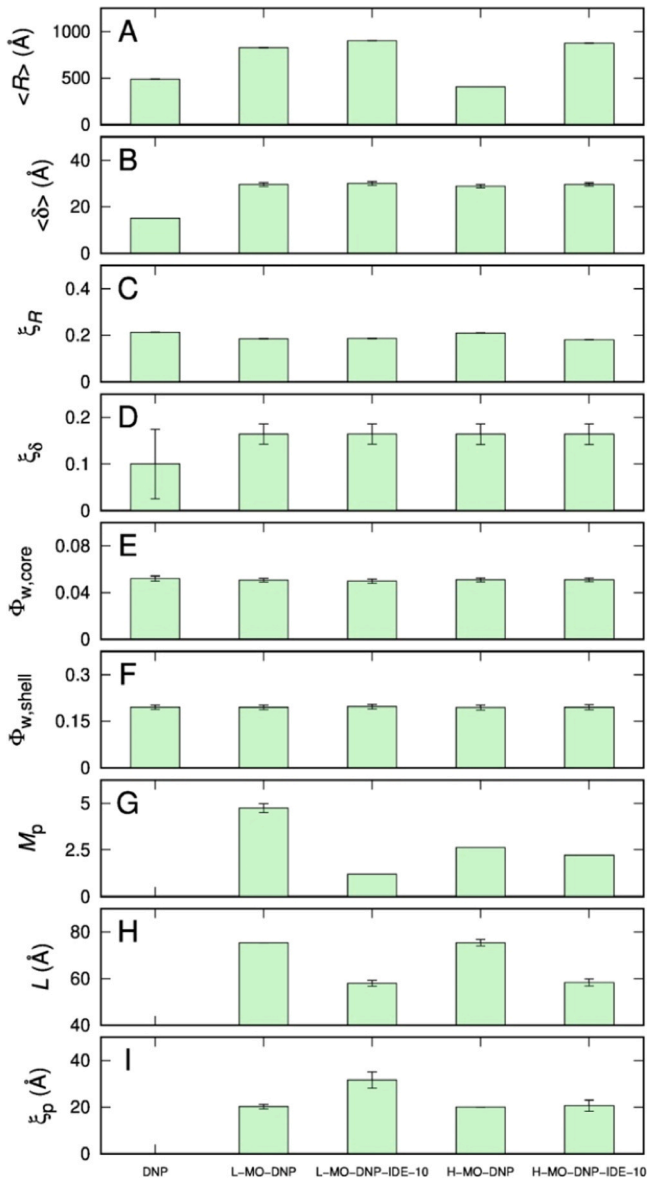

Fig. 6. Histograms of the most relevant fitting parameters derived from the analysis of the SAXS data in Fig. 5: (**A**) average radius of the sphere; (**B**) average shell thickness; (**C**) dispersion of the sphere radius; (**D**) dispersion of the shell thickness; (**E**) water fraction in the core domain; (**F**) water fraction in the shell domain; (**G**) correlation peak height-to-background ratio; (**H**) sponge cell dimension; (**I**) peak correlation length.

not exhibit significative intrinsic antioxidant properties, since the % decrease of [DMPO-HO]$^{\bullet}$ adduct is 8 % concerning control. The reason for the very small decrease of EPR signal in H-MO-DNP with respect to the control solution is ascribed to the polymer chains, that being amorphous, could statistically exhibit sporadic events of H transfer or electron transfer. Concerning the solution with only the IDE, the quinone lowered the amount of DMPO radical adduct by about 14 % concerning control underlining the ability of IDE to scavenge OH$^{\bullet}$. A molar concentration of 1.91×10^{-6} M for the [DMPO-HO]$^{\bullet}$ adduct was found (Table S2). Finally, the [DMPO-OH.] adduct was quantified in the other two solutions in which DNP-IDE were prepared in the presence of low and high MO concentrations (H-MO-DNP-IDE-10 and L-MO-DNP-IDE-10, respectively). In both, a decrease of about 40 % of radical adduct was observed (Fig. 7**C**). More in details, an adduct molar concentration of 1.69×10^{-6} M and 1.65×10^{-6} M was found for the H-MO-DNP-IDE-10 and L-MO-DNP-IDE-10, respectively. From these

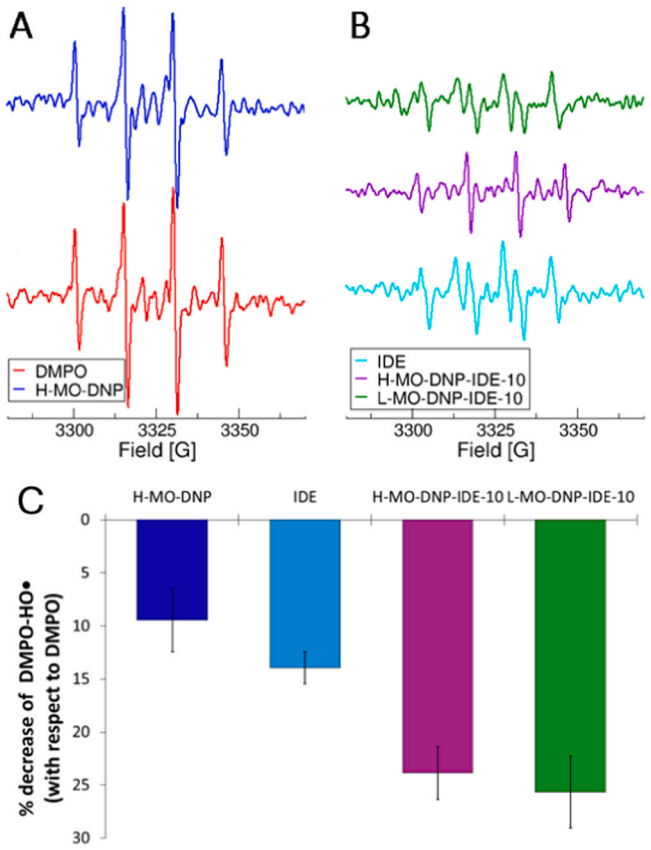

Fig. 7. EPR spectra of control (solution with only DMPO, and H-MO-DNP (**A**) EPR results for IDE, H-MO-DNP-IDE, and L-MO-DNP-IDE have also been reported (**B**) Percentage decrease of [DMPO-OH$^{\cdot}$] adduct in each system with respect to control (**C**).

results, it's clear that the presence of the entire formulation maximizes the antioxidant potential of the IDE. This is consistent considering the high lipophilicity of IDE which led to the aggregation phenomena in solutions, preventing therefore an efficient radical scavenging.

Even if this result confirms a good activity of IDE to react with OH$^{\bullet}$ radical, its intrinsic antioxidant capabilities remain unclear, and results in the literature show contradictory results. In fact, IDE is a lipophilic electron carrier and endogenous antioxidant. In the mitochondrial inner membrane, it is known to transfer electrons to complex III of the electron transport chain. Moreover, IDE can also act as a pro-oxidant generating an unstable semiquinone at complex I. In this respect, DFT approach was then used to identify the highest occupied molecular orbitals (HOMO) and the lowest unoccupied molecular orbitals (LUMO), and then to propose a mode of antioxidant action for this molecule. Moreover, since IDE exhibits different oxidation states, each form was analyzed.

The frontier molecular orbitals (FMO) for the ground state of IDE are shown in Fig. 8. From these results, both orbitals were substantially distributed over the conjugation plane of each IDE form and on the groups which are near the aromatic function. More in detail, regarding the Quinone form (Fig. 8**A**), the electronic transitions and the electron cloud of the HOMO were delocalized on the O atoms of OCH_3 groups, and the side of the aromatic ring close to these atoms. For comparison, the LUMO was mainly delocalized on the remaining portion of the aromatic ring, and particularly on the carbonyl oxygen atoms. This confirms the tendency of IDE to undergo a two-electron reduction, generating the Hydroquinone form (Fig. 8**B**). Focusing on this reduced form, a redistribution of HOMO was evident throughout the aromatic ring, with a peculiar involvement of the hydroxyl O positioned near the aliphatic chain. On the other hand, the LUMO was distributed more homogeneously on the aromatic ring, without any relevant involvement

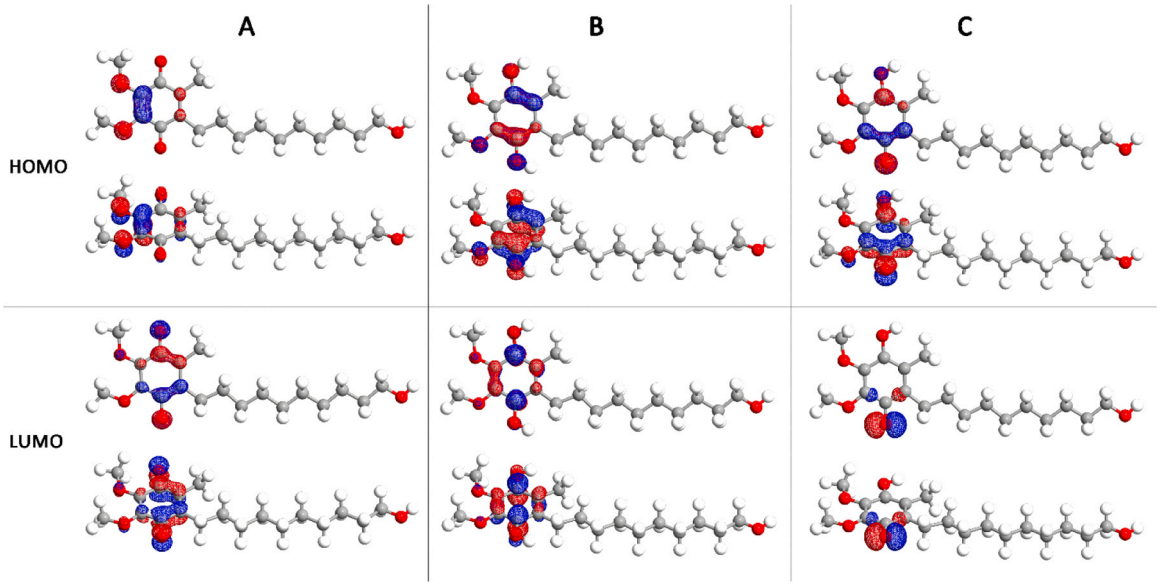

Fig. 8. The highest occupied molecular orbital (HOMO) and the lowest unoccupied molecular orbital (LUMO) of the Quinone (**A**), Hydroquinone (**B**), and Semiquinone (**C**) forms of IDE.

of the O atoms. From these results, it can be noticed that the two reduced O atoms were not equivalent, on the contrary, the group near the chain appeared much more reactive than the other one, and this led to the description of the Semiquinone form, in which radical species was mainly localized on the corresponding O atom (Fig. 8**C**). Analyzing the HOMO-LUMO distribution on the third form, the role of the above-mentioned oxygen appeared clear. Determining how Hydroxyquinone inherently donates its hydrogen atom to radicals, the phenolic part of the molecule reacts directly with a free radical, which is neutralized, and a radical form of phenolic antioxidant appears. To confirm this trend, the bond-dissociation enthalpy (BDH) was calculated, since it represents the numerical parameter associated with this antioxidant mechanism. A lower BDH parameter is correlated to a higher tendency to perform HAT. According to the Mulliken charges for IDE forms, the hydroxyl group near the aliphatic chain can release H much better than the one near the methyl group. Indeed, the first O exhibits a Mulliken charge of −0.428, while the second one has a value of −0.144.

Altogether, these results show that IDE doesn't exhibit strong antioxidant activity, but the unique antioxidant behavior is guaranteed by its reduced form, i.e. hydroquinone. Indeed, in this form, it can impair lipid peroxidation and detoxify a wide variety of free radicals performing HAT reactions, and this is the reason for the decreased [DMPO-OH]$^{\bullet}$ concentration. Furthermore, the L-DNP and H-DNP formulations do not affect the antioxidant properties of IDE, on the contrary, by preventing aggregation with itself, the overall protection effect from OH$^{\bullet}$ radical is greater than the effectiveness of the molecule without formulation.

3.5. *Intracellular ROS Scavenging in dermal fibroblasts*

The newly produced formulation was finally tested in a cellular model of oxidative stress to assess its potential application for the treatment of skin disorders associated with an increase in intracellular ROS production such as skin fibrosis [42], psoriasis [43], vitiligo [44], and atopic dermatitis [45]. Dermal fibroblasts play a crucial role in the development of these skin diseases, as well as in the ageing process [20], leading researchers to develop advanced drug delivery technologies and formulations capable of reducing intracellular ROS levels [46]. Additionally, it is known that the accumulation of hydrogen peroxide can be utilized to differentiate between healthy and inflamed tissues [47]. Therefore, to study the efficacy of our IDE-loaded NPs and to determine the effect of varying MO concentrations, a human dermal fibroblast (HDF) cell system treated with H_2O_2 was used as a model. ROS quantification was performed by flow cytometry using the DCFDA fluorescent probe and the results showed as the % ROS Positive with respect to unstressed cells. All data derived from flow cytometry analyses was shown in Table S3. Based on cytotoxicity profiles (Fig. 9**A**), the HDF cells were treated with free IDE, L-MO-DNP-IDE-10 and H-MO-DNP-IDE-10 at final IDE and NPs concentration of 4 μM and 9 μg/mL, respectively following by treatment with H_2O_2. It is important to note that in our experimental condition, cell washing with PBS was performed prior to the addition of oxidant to ensure that only the systems entering the cell was able to act as a ROS scavenger. As shown in Fig. 9**B-C**, treatment with H_2O_2 induced an increase in ROS production of 40 % with respect to negative control.

IDE alone was able to reduce ROS levels by approximately 20 % compared to cells treated with hydrogen peroxide alone (% ROS positive, 26 % IDE+ H_2O_2 vs. 43 % H_2O_2). Encapsulation in NPs results in increased ability of IDE to scavenge generated free radicals. However, the amount of MO present in the NPs seems to influence the efficacy of the formulation. Indeed, the presence of high concentrations of MO results in a reduction of free radicals 4-times and 2-times higher with respect to positive control and IDE alone, respectively (% ROS positive, 10 % H-MO-DNP-IDE-10 + H_2O_2 *vs.* 43 % H_2O_2 and 26 % IDE). In this case, ROS levels are reduced to values approaching those of cells not treated with H_2O_2. The system prepared with low MO concentrations demonstrated a greater ability to scavenge ROS compared to IDE; however, it was less effective than H-MO-DNP-IDE-10 (% ROS positive, 10 % H-MO-DNP-IDE-10 + H_2O_2 vs 17 % L-MO-DNP-IDE-10 + H_2O_2). This could be related to a greater uptake of the NPs inside the cells due to the presence of a more uniform surface lipid layer present in the H-MO-DNP-IDE10 systems. In any case, both NPs showed higher ROS-scavenging capacity than IDE alone, highlighting their powerful potential to reduce intracellular ROS levels in dermal fibroblasts.

To better explain the increased ability of IDE-NPs to protect against ROS respect to potency of the IDE alone, snapshots of MD simulations were reported (Figure S3). Analysing the system with IDE alone, a stable aggregate between different Quinone molecules is generated with evident π-stacking phenomena between the aromatic components of molecules, pairing in a staggered manner into dimers. This stable aggregate decreases the availability of the aromatic component of the molecule, which is therefore less inclined to exert the oxidation-

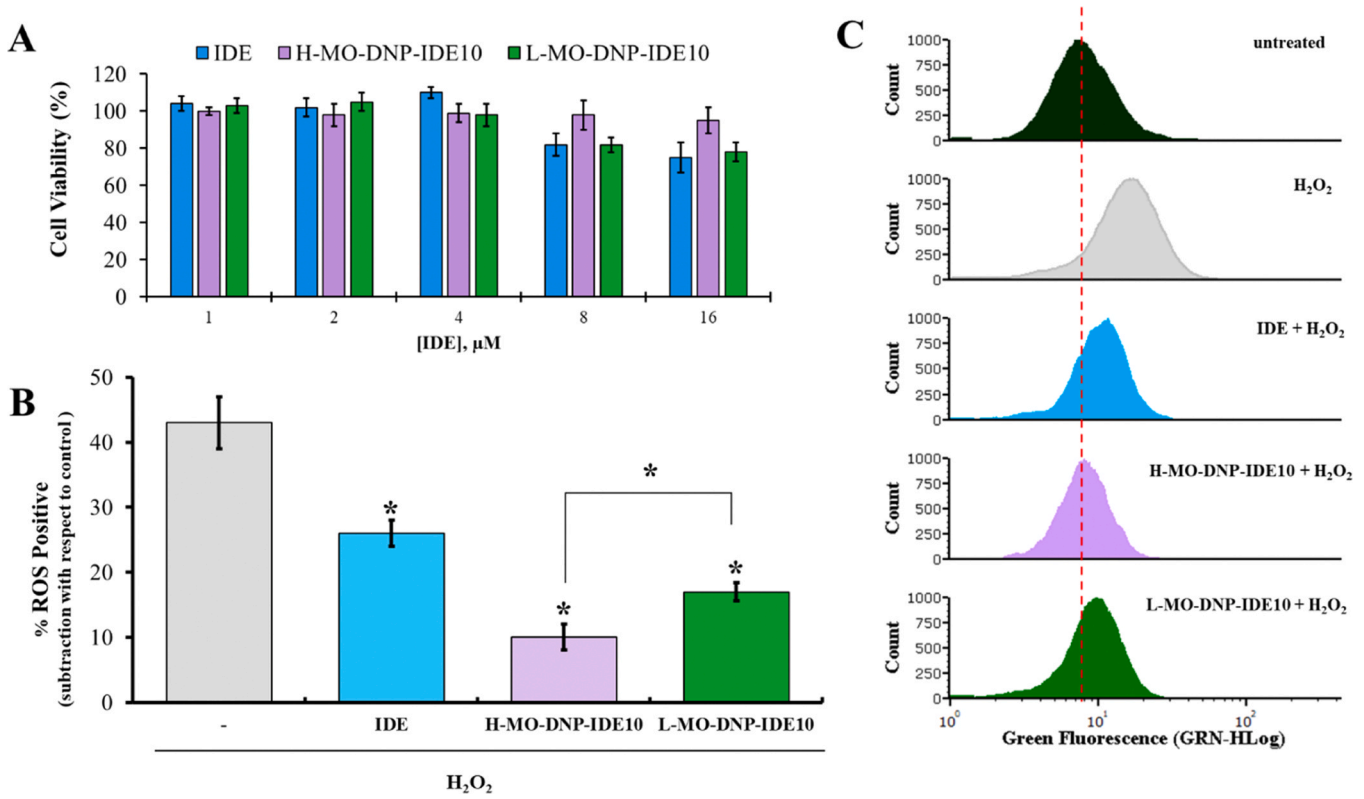

Fig. 9. ROS Scavenging in human dermal fibroblasts (HDF). **(A)** Cytotoxicity of IDE alone, H-MO-DNP-IDE-10 and L-MO-DNP-IDE-10 in HDF cell culture after 24 h of incubation. **(B)** Hystogram showing the % ROS Positive cells after treatment with IDE alone, H-MO-DNP-IDE-10 and L-MO-DNP-IDE-10 for 3 h followed by 1 mM H_2O_2 treatment for 1 h. ROS levels were measured by flow cytometry analyses with the DCFH-DA dye (FL1 channel, Ex: 488 nm/Em: 519 nm). Results are reported by using histogram subtraction statistics tool in FCS 7 Express with untreated cells as control (% Positive cells with respect to control). **(C)** Representative flow cytometric images of HDF in the conditions tested. The number of cells is plotted versus the DCFH fluorescence detected by the FL-1 channel. *P < 0.05.

reduction effect with which IDE protects against ROS. On the other hand, the presence of MO and DSPE-PEG_{2000} in PLGA NP has the role to disperse IDE molecules in the periphery of the polymer medium, avoiding quinone aggregates. More, the MO interacts with IDE through apolar interactions between the aliphatic chains and an hydrogen bond between a hydroxyl group of MO and the ketone oxygen of IDE. These interactions between MO and IDE lead to the orientation of the aromatic heads outside the PLGA surface, making the molecule more effective to intercept ROS.

4. Conclusions

In this study we presented mixed PLGA-lipid nanoparticles that exhibit high protection activity from ROS, then enabling cell protection. The encapsulation of IDE in PLGA NPs offers many potential advantages for drug delivery, anyway, it also presents several technical and practical challenges. Addressing these limitations requires careful formulation development, thorough characterization, and rigorous testing to ensure the safety and efficacy of the final product. For this purpose, we used a combined *in silico* and *in vitro* approach based on the use of many different techniques to test the effects of two lipid stabilizers as DSPE-PEG_{2000} and MO on PLGA-IDE NPs. These lipid stabilizers exhibited key roles in increasing the stability of NPs and on the same time guaranteeing prominent antioxidant activity. In detail, AFM and DLS results show that MO determined the size and the shape of lipid–polymer NPs from a quantitative and a qualitative point of view, since different MO concentrations were tested. SAXS and MD evidenced the tendency of MO to directly interact with IDE, which, without this lipid stabilizer, would tend to aggregate and dimerize with itself, thus compromising the possibility of exploiting its antioxidant properties. MO was thus able to provide a more advantageous IDE arrangement inside the peripheral region of PLGA NPs, and in this way, the nanoformulations maintained high protective effect from $OH^{\cdot}$ radicals as confirmed by EPR and DFT analysis. Both DNP-IDE formulations with high and low MO concentration were efficient in the ROS scavenging activity observed using cytotoxicity and flow cytometry analyses, with an higher protection rate than that of IDE alone. The increased scavenging ability protects cells from oxidative stress because the NPs with the correct components enhances the IDE's adsorption. The results show how it is possible to determine the best formulation conditions to get most of the properties of molecules known as IDE, arriving at optimal, stable, non-toxic formulations, which allow the development of applications which are targeted to diseases caused by oxidative stress.

CRediT authorship contribution statement

Spinozzi Francesco: Resources, Data curation. **Moretti Paolo:** Visualization, Data curation. **Mobbili Giovanna:** Writing – original draft, Investigation. **Romagnoli Elena:** Writing – original draft, Data curation. **Pavoni Eleonora:** Software, Methodology. **Mohebbi Elaheh:** Software, Conceptualization. **Romaldi Brenda:** Investigation, Formal analysis. **Armeni Tatiana:** Resources, Investigation. **Stipa Pierluigi:** Writing – review & editing, Visualization, Supervision. **Laudadio Emiliano:** Writing – review & editing, Writing – original draft, Validation, Supervision, Project administration, Methodology, Formal analysis, Data curation, Conceptualization. **Minnelli Cristina:** Writing – review & editing, Writing – original draft, Methodology, Formal analysis, Conceptualization.

Declaration of Competing Interest

The authors declare that they have no known competing financial

interests or personal relationships that could have appeared to influence the work reported in this paper.

Appendix A. Supporting information

Supplementary data associated with this article can be found in the online version at doi:10.1016/j.colsurfa.2025.136864.

Data Availability

No data was used for the research described in the article.

References

[1] C. Minnelli, P. Stipa, G. Mobbili, S. Sabbatini, B. Romaldi, T. Armeni, E. Laudadio, Integration of lipid-functionalized epigallocatechin-3-gallate into PLGA matrix as a novel polyphenol-based nanoantioxidant, ACS Omega 8 (2023) 48292–48303, https://doi.org/10.1021/acsomega.3c07637.

[2] C. Minnelli, P. Moretti, E. Laudadio, Y. Gerelli, A. Pigozzo, T. Armeni, R. Galeazzi, P. Mariani, G. Mobbili, Tuning curvature and phase behavior of monoolein bilayers by epigallocatechin-3-gallate: Structural insight and cytotoxicity, Colloids Surf. B Biointerfaces 209 (2022) 112171, https://doi.org/10.1016/j.colsurfb.2021.112171.

[3] C. Minnelli, P. Stipa, S. Sabbatini, P. Mengucci, G. Mobbili, R. Galeazzi, T. Armeni, B. Romaldi, A. Celli, E. Laudadio, Insights into PLGA-encapsulated epigallocatechin 3-gallate nanoparticles as a new potential biomedical system: a computational and experimental approach, Eur. Polym. J.,182 (2023) 111723, https://doi.org/10.1016/j.eurpolymj.2022.111723.

[4] H.C. Huang, S. Barua, G. Sharma, S.K. Dey, K. Rege, Inorganic nanoparticles for cancer imaging and therapy, JCR 155 (2011) 344–357, https://doi.org/10.1016/j.jconrel.2011.06.004.

[5] B.S. Pattni, V.V. Chupin, V.P. Torchilin, New developments in liposomal drug delivery, Chem. Rev. 115 (2015) 10938–10966, https://doi.org/10.1021/acs.chemrev.5b00046.

[6] K. Ulbrich, K. Holá, V. Šubr, A. Bakandritsos, J. Tuček, R. Zbořil, Targeted drug delivery with polymers and magnetic nanoparticles: covalent and noncovalent approaches, release control, and clinical studies, Chem. Rev. 116 (2016) 5338–5431, https://doi.org/10.1021/acs.chemrev.5b00589.

[7] M.A. Beach, U. Nayanathara, Y. Gao, C. Zhang, Y. Xiong, Y. Wang, G.K. Such, Polymeric nanoparticles for drug delivery, Chem. Rev. 124 (2024) 5505–5616, https://doi.org/10.1021/acs.chemrev.3c00705.

[8] T. Urbánek, E. Jäger, A. Jäger, M. Hrubý, Selectively biodegradable polyesters: nature-inspired construction materials for future biomedical applications, Polymers 11 (2019) 1061, https://doi.org/10.3390/polym11061061.

[9] P. Grossen, D. Witzigmann, S. Sieber, J. Huwyler, PEG-PCL-based nanomedicines: a biodegradable drug delivery system and its application, JCR 260 (2017) 46–60, https://doi.org/10.1016/j.jconrel.2017.05.028.

[10] H.K. Makadia, S.J. Siegel, Poly lactic-co-glycolic acid (PLGA) as biodegradable controlled drug delivery carrier, Polym. (Basel) 3 (2011) 1377, https://doi.org/10.3390/polym3031377.

[11] X. Qi, S. Zhou, H. Fang, S. Yang, C. Hang, Y. Tian, C. Wang, One-step PDA coating strategy on pure Zn for blood-contacting engineering, J. Mater. Sci. Technol. 123 (2022) 78–91, https://doi.org/10.1016/j.jmst.2021.12.076.

[12] Y. Hao, R. Tian, K. Lv, Z. Liu, J. Ni, P. Yuan, Y. Bai, X. Chen, Stimuli responsive co-delivery of celecoxib and BMP2 from micro-scaffold for periodontal disease treatment, J. Mater. Sci. Technol. 75 (2021) 216–224, https://doi.org/10.1016/j.jmst.2020.10.027.

[13] X. Meng, L. Li, C. Huang, K. Shi, Q. Zeng, C. Wen, S. Grad, M. Alini, L. Qin, X. Wang, Anti-inflammatory and anabolic biphasic scaffold facilitates osteochondral tissue regeneration in osteoarthritic joints, J. Mater. Sci. Technol. 156 (2023) 20–31, https://doi.org/10.1016/j.jmst.2023.01.035.

[14] M. Bodmer, P. Vankan, M. Dreier, K.W. Kutz, J. Drewe, Pharmacokinetics and metabolism of idebenone in healthy male subjects, Eur. J. Clin. Pharm. 65 (2009) 493–501, https://doi.org/10.1007/S00228-008-0596-1.

[15] I. Zs.-Nagy, Chemistry, toxicology, pharmacology and pharmacokinetics of idebenone: a review, Arch. Gerontol. Geriatr. 11 (1990) 177–186, https://doi.org/10.1016/0167-4943(90)90063-C.

[16] N. Gueven, K. Woolley, J. Smith, Border between natural product and drug: comparison of the related benzoquinones idebenone and coenzyme Q10, Redox Biol. 4 (2015) 289–295, https://doi.org/10.1016/j.redox.2015.01.009.

[17] S. Shastri, T. Shinde, R. Eri, S.S. Sohal, N. Gueven, Idebenone protects against acute murine colitis via antioxidant and anti-inflammatory mechanisms, Int J. Mol. Sci. 21 (2020) 484, https://doi.org/10.3390/ijms21020484.

[18] P. Lin, J. Liu, M. Ren, K. Ji, L. Li, B. Zhang, Y. Gong, C. Yan, Idebenone protects against oxidized low density lipoprotein induced mitochondrial dysfunction in vascular endothelial cells via GSK3β/β-catenin signalling pathways, Biochem Biophys. Res Commun. 465 (2015) 548–555, https://doi.org/10.1016/j.bbrc.2015.08.058.

[19] W. Jiang, H. Geng, X. Lv, J. Ma, F. Liu, P. Lin, C. Yan, Idebenone Protects against Atherosclerosis in Apolipoprotein E-Deficient Mice Via Activation of the SIRT3-SOD2-mtROS Pathway, Cardiovasc Drugs Ther. 35 (2021) 1129–1145, https://doi.org/10.1007/s10557-020-07018-5.

[20] D. McDaniel, B. Neudecker, J. DiNardo, J. Lewis, H. Maibach, Clinical efficacy assessment in photodamaged skin of 0.5% and 1.0% idebenone, J. Cosmet. Dermatol. 4 (2005) 167–173, https://doi.org/10.1111/j.1473-2165.2005.00305.x.

[21] J.E. Oblong, A. Bowman, H.A. Rovito, B.B. Jarrold, J.D. Sherrill, M.R. Black, G. Nelson, A.B. Kimball, M.A. Birch-Machin, Metabolic dysfunction in human skin: Restoration of mitochondrial integrity and metabolic output by nicotinamide (niacinamide) in primary dermal fibroblasts from older aged donors, Aging Cell 19 (2020), https://doi.org/10.1111/acel.13248.

[22] W. Wan, A.Dawn Bannerman, L. Yang, H. Mak, Poly(Vinyl Alcohol) Cryogels for Biomedical Applications, Adv. Polym. Sci. 263 (2014) 283–321, https://doi.org/10.1007/978-3-319-05846-7_8.

[23] F. Spinozzi, C. Ferrero, M.G. Ortore, A. De Maria Antolinos, P. Mariani, GENFIT: Software for the analysis of small-angle X-ray and neutron scattering data of macro-molecules in solution, J. Appl. Crystallogr 47 (2014) 1132–1139, https://doi.org/10.1107/S1600576714005147.

[24] B. Angelov, A. Angelova, R. Mutafchieva, S. Lesieur, U. Vainio, V.M. Garamus, G. V. Jensen, J.S. Pedersen, SAXS investigation of a cubic to a sponge (L3) phase transition in self-assembled lipid nanocarriers, Phys. Chem. Chem. Phys. 13 (2011) 3073–3081, https://doi.org/10.1039/c0cp01029d.

[25] F. Spinozzi, P. Moretti, D.R. Perinelli, G. Corucci, P. Piergiovanni, H. Amenitsch, G. A. Sancini, G. Franzese, P. Blasi, Small-angle X-ray scattering unveils the internal structure of lipid nanoparticles, J. Colloid Interface Sci. 662 (2024) 446–459, https://doi.org/10.1016/j.jcis.2024.02.076.

[26] I. Clemente, S. Falsini, E. Di Cola, G.C. Fadda, C. Gonnelli, F. Spinozzi, M. Bacia-Verloop, I. Grillo, S. Ristori, Green nanovectors for phytodrug delivery: In-depth structural and morphological characterization, ACS Sustain Chem. Eng. 7 (2019) 12838–12846, https://doi.org/10.1021/acssuschemeng.9b01748.

[27] A. Jakalian, D.B. Jack, C.I. Bayly, Fast, efficient generation of high-quality atomic charges. AM1-BCC model: II. Parameterization and validation, J. Comput. Chem. 23 (2002) 1623–1641, https://doi.org/10.1002/jcc.10128.

[28] P. Mark, L. Nilsson, Structure and Dynamics of the TIP3P, SPC, and SPC/E Water Models at 298 K, J. Phys. Chem. B 105 (2001) 9954–9960, https://doi.org/10.1021/jp003020w.

[29] B. Kohnke, C. Kutzner, H. Grubmüller, A GPU-Accelerated Fast Multipole Method for GROMACS: Performance and Accuracy, J. Chem. Theory Comput. 16 (2020) 6938–6949, https://doi.org/10.1021/acs.jctc.0c00744.

[30] Y. Yu, A. Krämer, R.M. Venable, B.R. Brooks, J.B. Klauda, R.W. Pastor, CHARMM36 Lipid Force Field with Explicit Treatment of Long-Range Dispersion: Parametrization and Validation for Phosphatidylethanolamine, Phosphatidylglycerol, and Ether Lipids, J. Chem. Theory Comput. 17 (2021) 1581–1595, https://doi.org/10.1021/acs.jctc.0c01327.

[31] E. Laudadio, R. Galeazzi, G. Mobbili, C. Minnelli, A. Barbon, M. Bortolus, P. Stipa, Depth Distribution of Spin-Labeled Liponitroxides within Lipid Bilayers: A Combined EPR and Molecular Dynamics Approach, ACS Omega 4 (2019) 5029–5037, https://doi.org/10.1021/acsomega.8b03395.

[32] B. Hess, H. Bekker, H.J.C. Berendsen, J.G.E.M. Fraaije, LINCS: A Linear Constraint Solver for molecular simulations, J. Comp. Chem. 18 (1997) 1463–1472, https://doi.org/10.1002/(sici)1096-987x(199709)18:12< 1463::aid-jcc4> 3.0.co;2-h.

[33] R. Zhang, C. Gao, S. Pan, R. Shang, Fusion of GNSS and Speedometer Based on VMD and Its Application in Bridge Deformation Monitoring, Sensors 20 (2020) 694, https://doi.org/10.3390/S20030694.

[34] E.F. Pettersen, T.D. Goddard, C.C. Huang, G.S. Couch, D.M. Greenblatt, E.C. Meng, T.E. Ferrin, UCSF Chimera - A visualization system for exploratory research and analysis, J. Comput. Chem. 25 (2004) 1605–1612, https://doi.org/10.1002/jcc.20084.

[35] E. Klein, V. Lukeš, M. Ilčin, DFT/B3LYP study of tocopherols and chromans antioxidant action energetics, Chem. Phys. 336 (2007) 51–57, https://doi.org/10.1016/j.chemphys.2007.05.007.

[36] N.P. Morales, S. Sirijaroonwong, P. Yamanont, C. Phisalaphong, Electron Paramagnetic Resonance Study of the Free Radical Scavenging Capacity of Curcumin and Its Demethoxy and Hydrogenated Derivatives, Biol. Pharm. Bull. 38 (2015) 1478–1483, https://doi.org/10.1248/bpb.b15-00209.

[37] R. Varela-Fernández, C. Bendicho-Lavilla, M. Martin-Pastor, R. Herrero Vanrell, M. I. Lema-Gesto, M. González-Barcia, F.J. Otero-Espinar, Design, optimization, and in vitro characterization of idebenone-loaded PLGA microspheres for LHON treatment, Int J. Pharm. 616 (2022) 121504, https://doi.org/10.1016/j.ijpharm.2022.121504.

[38] C. Morilla-Lomeña, B. Reguera-Insausti, V. Andrés-Guerrero, M.V. de la Torre, M. Brugnera, B. de las Heras, R. Herrero-Vanrell, I. Cuadrado-Berrocal, I. Bravo-Osuna, Idebenone addition in protein-loaded PLGA / VitE microspheres as neuroprotective IODDS, Acta Ophthalmol. 102 (S279) (2024), https://doi.org/10.1111/aos.16213.

[39] D. Marsh, Molecular volumes of phospholipids and glycolipids in membranes, Chem. Phys. Lipids 163 (2010) 667–677, https://doi.org/10.1016/j.chemphyslip.2010.06.005.

[40] Online source: https://www.chemicalbook.com/ChemicalProductProperty_EN_CB7733840.htm

[41] B. Yang, J.P. Lowe, R. Schweins, K.J. Edler, Small angle neutron scattering studies on the internal structure of poly(lactide- co -glycolide)- block -poly(ethylene glycol) nanoparticles as drug delivery vehicles, Biomacromolecules 16 (2015) 457–464, https://doi.org/10.1021/bm501519u.

[42] A. Shroff, A. Mamalis, J. Jagdeo, Oxidative Stress and Skin Fibrosis, Curr. Pathobiol. Rep. 2 (2014) 257–267, https://doi.org/10.1007/s40139-014-0062-y.

[43] J. Hu, Q. Bian, X. Ma, Y. Xu, J. Gao, A double-edged sword: ROS related therapies in the treatment of psoriasis, Asian J. Pharm. Sci. 17 (2022) 798–816, https://doi.org/10.1016/j.ajps.2022.10.005.

[44] Y. Xuan, Y. Yang, L. Xiang, C. Zhang, The Role of Oxidative Stress in the Pathogenesis of Vitiligo: A Culprit for Melanocyte Death, Oxid. Med Cell Longev. 2022 (2022) 8498472, https://doi.org/10.1155/2022/8498472.
[45] N. Sivaranjani, S. Venkata Rao, G. Rajeev, Reactive oxygen species (ROS), Oxidative stress, Antioxidants, Atopic dermatitis, JCDR 7 (2013) 2683–2685, https://doi.org/10.7860/jcdr/2013/6635.3732.
[46] H. Ye, Y. Zhou, X. Liu, Y. Chen, S. Duan, R. Zhu, Y. Liu, L. Yin, Recent Advances on Reactive Oxygen Species-Responsive Delivery and Diagnosis System, Biomacromolecules 20 (2019) 2441–2463, https://doi.org/10.1021/acs.biomac.9b00628.
[47] H. Sies, Hydrogen peroxide as a central redox signaling molecule in physiological oxidative stress: Oxidative eustress, Redox Biol. 11 (2017) 613–619, https://doi.org/10.1016/J.redox.2016.12.035.